Redox-Dependent Dynamics in Cytochrome P450$_{cam}$[†]

Susan Sondej Pochapsky,[‡] Marina Dang,[‡] Bo OuYang,[‡] Alana K. Simorellis,[‡] and Thomas C. Pochapsky*[‡,§]

[‡]*Department of Chemistry and* [§]*Department of Biochemistry and Rosenstiel Basic Medical Science Research Institute, Brandeis University, 415 South Street, MS 015, Waltham, Massachusetts 02454-9110*

Received January 2, 2009; Revised Manuscript Received March 30, 2009

ABSTRACT: Local protein backbone dynamics of the camphor hydroxylase cytochrome P450$_{cam}$ (CYP101) depend upon the oxidation and ligation state of the heme iron. ^{1}H$-^{15}$N correlation nuclear magnetic resonance experiments were used to compare backbone dynamics of oxidized and reduced forms of this 414-residue metalloenzyme via hydrogen$-$deuterium exchange kinetics (H$-$D exchange) and ^{15}N relaxation measurements, and these results are compared with previously published results obtained by H$-$D exchange mass spectrometry. In general, the reduced enzyme exhibits lower-amplitude motions of secondary structural features than the oxidized enzyme on all of the time scales accessible to these experiments, and these differences are more pronounced in regions of the enzyme involved in substrate access to the active site (B′ helix and β3 and β5 sheets) and binding of putidaredoxin (C and L helices), the iron$-$sulfur protein that acts as the effector and reductant of CYP101 in vivo. These results are interpreted in terms of local structural effects of changes in the heme oxidation state, and the relevance of the observed effects to the enzyme mechanism is discussed.

The dynamics of any protein, be it structural, regulatory, or enzymatic, must be taken into consideration when trying to understand biological function. Metalloproteins provide excellent models for the role of protein dynamics in function, particularly if discrete changes in oxidation state or the identity of the bound metal plays a role in modulating function. We and others have described cases in which the identity of a bound metal is critical in determining protein structure and dynamics and provides a mechanism for selective metal sensing (*1, 2*). Alternatively, a tightly bound metal cofactor (such as a heme or Fe$-$S cofactor) can change oxidation state as either a sensor (*3*) or an integral step in redox chemistry. We have observed redox-dependent modulation of the structure and dynamics of the Cys$_4$Fe$_2$S$_2$ ferredoxin putidaredoxin (Pdx),[1] which serves as the electron transfer partner and effector of cytochrome P450$_{cam}$ (CYP101) from *Pseudomonas putida* (*4*). CYP101 catalyzes the 5-exo hydroxylation of the monoterpene camphor by molecular oxygen in the first step of camphor catabolism by *P. putida*. The process requires two electrons, both of which are obtained by oxidation of NADH. NADH oxidation is catalyzed by the flavoprotein putidaredoxin reductase (PdR), and the electrons generated thereby are transferred in sequential one-electron steps from PdR to CYP101 by Pdx. While the first electron transfer to CYP101 is nonspecific and can be accomplished by any reductant of suitable potential, productive electron transfer in the second step is tightly coupled to an effector-driven conformational change that generates the enzymatically competent conformation of CYP101. We have recently described evidence for a specific X-Pro cis$-$trans isomerization in reduced CYP101 that is triggered by the binding of reduced Pdx (Pdx^r), and which appears to account for the structural perturbations observed upon complex formation (*5*).

It is clear that redox-dependent modulation of Pdx$-$CYP101 interactions takes place: the interaction between oxidized Pdx (Pdx^o) and oxidized CYP101 is weaker than that of the reduced forms of proteins and does not produce the conformational changes observed in the reduced$-$reduced complex as detected by NMR spectroscopy (*6*). It has been shown that, besides constraining protein dynamics, reduction of Pdx results in population of fewer conformational substates than the oxidized protein (*7*). We proposed that this is the mechanism by which the binding affinity of Pdx and CYP101 is modulated: If the subset of conformational states occupied by reduced Pdx (Pdx^r) is the same as that selected upon binding to CYP101, much of the entropic cost of binding Pdx to CYP101 is "prepaid", with concomitant lowering of the binding free energy.

We expect this mechanism to be a two-way street: If CYP101 is more conformationally constrained after one-electron reduction, this reduces conformational entropy, making a specific interaction between Pdx and CYP101 energetically more favorable prior to the second electron transfer. Furthermore, "stiffening"

CYP101 would provide the mechanical coupling necessary to transmit the forces exerted by Pdx at the proximal binding interface to the relatively remote distal regions of CYP101, where changes are observed in the enzymatically competent complex (5). We have found evidence from hydrogen−deuterium (H−D) exchange mass spectrometry that a number of regions of CYP101 that are involved in binding Pdx and/or modulating substrate access and orientation in the active site have lower-amplitude motions in the reduced form than in oxidized CYP101 on the time scale of 10^1-10^3 s (8). We now show that ^{15}N relaxation as well as H−D exchange as monitored by NMR provides a complement to the mass spectrometric data, and the combination of methodologies allows local comparison of dynamic behavior between two oxidation states of CYP101 on several time scales.

MATERIALS AND METHODS

Expression and Purification of CYP101. Overexpression and purification of CYP101 were conducted as previously described (6, 21). The plasmid for C334A CYP101 was transformed into chemically competent *Escherichia coli* NCM533 cells. The C334A mutant of CYP101 is identical spectroscopically and enzymatically to wild-type (WT) CYP101 but does not dimerize in solution at high concentrations (22). Transformants were selected on the basis of chloroamphenicol and kanamycin resistance. Colonies were grown in M9 medium containing trace metals (M9+) at 37 °C with the sole nitrogen source being ^{15}NH$_4$Cl (Cambridge Isotope Laboratories, Andover, MA). The cells were grown to an optical density (OD$_{600}$) of 1.0, at which point they were induced with 1 mM IPTG. Additionally, 5 mM camphor and 70 mg of porphyrin precursor δ-aminolevulinic acid were added per liter of medium to improve the yield of folded CYP101. The cells were incubated for an additional 12 h after induction at 37 °C. Cells were harvested by centrifugation at 2700g and 4 °C and were stored frozen at −80 °C until they were purified. Perdeuterated [U-^{15}N] CYP101 was used for the ^{15}N relaxation experiments and was obtained using the procedure described above with the exception that 0.3% d_8-glycerol (Cambridge Isotope Laboratories) was used as the carbon source in D$_2$O-based M9 medium. ^{15}NH$_4$Cl and all inorganic salts were added from stock solutions in D$_2$O.

Cell paste containing CYP101 was thawed and sonicated in 50 mM Tris-HCl (pH 7.4), 1 mM camphor, and 50 mM KCl (buffer A). The extract was cleared by centrifugation at 20000g for 20 min and the pellet discarded. Protamine sulfate (10 mg/g of cell pellet) was slowly added to the supernatant, followed by centrifugation at 20000g for an additional 20 min, and the pellet was again discarded. Ammonium sulfate was slowly added to the supernatant to 70% saturation. The solution was then centrifuged at 20000g for 30 min. The resulting pellet was resuspended and dialyzed against buffer A overnight at 4 °C. The protein solution was diluted into 100 mL of L buffer and loaded onto a DEAE-Sepharose 20 mL fast flow column (Amersham Biosciences, Piscataway, NJ) followed by size exclusion on a P100 gravity column (Bio-Rad, Hercules, CA). The purity of the enzyme was determined by measuring absorption ratios (A_{391}/A_{280}) on a Hitachi U-2000 UV−visible spectrophotometer. The fractions with an absorption ratio of >1.4 were concentrated using an Amicon Ultra centrifugal filter concentrator (Millipore, Billerica, MA) until the protein

concentration exceeded 500 μM. The yield of the protein following purification was approximately 13 mg per liter of cell culture. The purified sample was frozen immediately in liquid nitrogen until it was needed.

Buffer Exchange Procedure. Ideally, NMR H−D exchange experiments make use of lyophilized protein that is rehydrated in deuterated buffer immediately prior to the experiment. We could not use this method because CYP101 is not stable to lyophilization. Instead, buffer exchange was accomplished using a spin column packed with P2 gel (Biorad) pre-equilibrated with a buffer containing 100 mM KCl, 50 mM d-Tris, and 2 mM camphor (pH 7.4). It is important to pre-equilibrate the column multiple times before exchange, as camphor has a tendency to adhere to the gel and can easily be removed from the sample by the exchange process. Furthermore, for CYP-S-CO, the buffer was degassed and saturated with carbon monoxide gas prior to equilibration of the spin column. For reference samples, the buffer was protonated with 10% D$_2$O for locking purposes. For the H−D exchange experiments, the buffer was made using 99.9% D$_2$O (Cambridge Isotope Laboratories); 800 μL of pre-equilibrated resin was washed nine times with equal parts buffer and spun for 1 min at 4000g. Subsequently, the protein was applied to the column and the column spun for 15 s at 4000g. The sample was recovered and sealed in an NMR Shigemi tube (Shigemi Inc., Allison Park, PA). The protein concentration prior to exchange was 0.6 mM. The concentration was not measured after exchange into D$_2$O buffer so the NMR experiments could be started immediately.

Reduction of CYP101. The CYP101 sample was placed under a carbon monoxide atmosphere. Aliquots of a sodium dithionite solution [0.25 M Na$_2$S$_2$O$_4$ and 1 M Tris-HCl (pH 8.0)] were added slowly to the sample until a clear red color was observed. The reduced camphor and CO-bound CYP101 (CYP-S-CO) was transferred to an anaerobic chamber where it was either placed directly into an NMR tube (reference spectrum) or exchanged into deuterated buffer as described above and placed in an NMR tube.

H−D Exchange NMR Measurements. H−D exchange for both CYP-S and CYP-S-CO was initiated by exchange into deuterated buffer as described above. Typically, there was an unavoidable 10 min delay between the start of exchange and return of the sample to the spectrometer. Shims were adjusted if required prior to starting the experimental series. ^{15}N TROSY-HSQC experiments were acquired in series for 33 h, with each experiment taking ~ 36 min to complete, yielding a total of 53 time points. Time points were assumed to reflect to sample condition at the end of each experiment. All experiments were recorded at 25 °C on a Bruker Avance 800 MHz spectrometer, equipped with z-gradient TCI cryoprobe, operating at 800.13 MHz (^{1}H) and 81.076 MHz (^{15}N). ^{15}N HSQC-TROSY experiments were conducted using a standard TROSY-based pulse sequence (23). Sixteen transients were acquired per t_1 point with 64 complex t_1 increments using an acquisition time of 0.07 s. Data were processed using Topspin (Bruker Biospin, Billerica, MA).

H−D Exchange Calculations. Correlations in the ^{15}N TROSY-HSQC spectrum corresponding to amide protons in the protein backbone were assigned as described in previous publications (5, 6, 21). As amide protons exchange with deuterons, the intensity of the corresponding correlation decreases. Integrated peak intensities of each correlation were measured using Topspin (Bruker Biospin). Integrated peak intensities were

then fitted using the LinearRegression package of *Mathematica* 6.0 (Wolfram Research) to the linear expression

$$\ln I = \ln I_{o} - R_{ex}t \qquad (1)$$

where I is the integrated signal intensity, I_{o} is the initial intensity of the resonance (obtained from the *y*-intercept of the fit), R_{ex} is the exchange rate, and t is time. The goodness of fit in most cases was improved by using the *Mathematica* routine MovingAverage, which replaces each original data point with the average of two adjacent points. This routine results in one fewer data point than in the original data set. For each peak, the goodness of fit was determined visually by plotting data points together with the fitted line (see the Supporting Information). In cases of relatively fast exchange, where back-exchange from an increasing concentration of ^{1}H in the buffer becomes a factor at later times, fits were visibly improved by only fitting the earlier time points. In all cases, the 68% confidence level was used to provide error estimates for the fits, and these levels are provided in Table 1.

Heteronuclear Relaxation Measurements. ^{15}N T_1 and T_2 values were determined using two-dimensional (2D) TROSY-based pulse sequences (*24*). Relaxation experiments were conducted at 25 °C on a Bruker Avance 800 MHz spectrometer, equipped with a z-gradient TCI cryoprobe, operating at 800.13 MHz (^{1}H) and 81.076 MHz (^{15}N). Spectral widths were 14367.8 Hz (^{1}H) and 3243.5 Hz (^{15}N). Two samples were employed: camphor-bound oxidized CYP101 (CYP-S) and reduced CO- and camphor-bound CYP101 (CYP-S-CO). Both samples were prepared in uniformly ^{15}N and perdeuterated form, 0.5 mM in a 90% H_2O/10% D_2O (pH 7.4) mixture, 50 mM *d*-Tris-HCl, 100 mM KCl, and 2 mM D-camphor. All spectra were processed, and peak intensities were measured using NMRPipe.

T_1 experiments were conducted with 32 scans per t_1 point, a 2.7 s recycle delay, and 102 (^{15}N) × 2048 (^{1}H) complex points in the CYP-S sample. The CYP-S-CO sample was run under identical conditions except 128 (^{15}N) × 2048 (^{1}H) complex points were acquired. For both samples, variable delays of 100, 200, 400, 800, 1600, and 2400 ms were used in an interleaved manner. Two of the time points (100 and 200 ms) were repeated to confirm reproducibility.

T_2 experiments were conducted with 40 scans per t_1 point, a 1 s recycle delay, and 128 (^{15}N) × 2048 (^{1}H) complex points. Variable delays of 0, 16, 32, 48, and 64 ms were used in an interleaved manner. Two of the time points (0 and 16 ms) were repeated to confirm reproducibility.

Peak intensities from relaxation data sets were normalized and fitted with two parameters, I_o and k, to eq 2 using the NonlinearRegress function of *Mathematica* 6.0 (Wolfram Research, Urbana, IL).

$$I = I_0 \exp(-kt) \qquad (2)$$

Error estimates for all relaxation data were taken at the 68% confidence level as calculated with NonlinearRegress.

RESULTS

Amide proton exchange provides a convenient means of monitoring local dynamics in folded proteins. To permit exchange, hydrogen bond donor−acceptor pairs involving amide protons must be separated by > 5 Å for a significant fraction of time by local fluctuations (*9*). The degree to which H−D exchange occurs during a time course experiment provides a
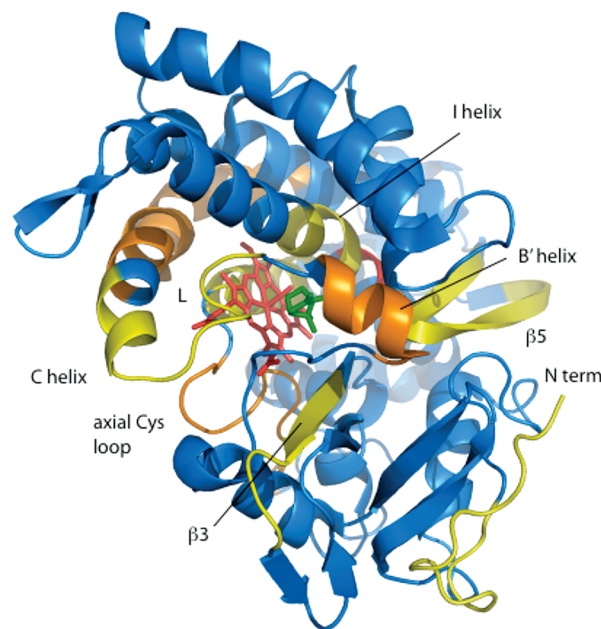

FIGURE 1: Differences in H−D exchange rates between oxidized CYP-S and reduced CYP-S-CO, determined by MS/MS as described previously, superimposed on the 3CPP structure of CYP101 (*8*, *25*). In all cases, H−D exchange was faster in CYP-S than in CYP-S-CO. The color scheme shows blue (< 5% difference) through yellow to red indicating the largest redox sensitivity for H−D exchange. Colored yellow (5−10% difference in H−D exchange rates) are residues 3−24 (N-terminus), 98−110 (C helix), 247−251 (I helix kink), and 297−304 in the β3 sheet. Colored orange (11−20% difference) are residues 88−95 (B′ helix), 113−134 (C helix), and 343−370 (the loop containing the axial heme ligand Cys 357 and portions of the L helix). The greatest difference (31%) was observed for residues 254−256 in the I helix, colored red. This figure was generated using PyMOL (*26*).

measure of the fraction of time such open states exist and hence the dynamic variations in local protein structure. H−D exchange can be measured by either NMR or mass spectrometry (MS). We recently described the use of tandem mass spectrometry (MS/MS) to detect redox-dependent differences in the extent of H−D exchange in peptide fragments of CYP101 (*8*). Figure 1 provides a summary of our observations from that work. In all cases where differences are seen, H−D exchange was faster in oxidized CYP-S than in reduced CYP-S-CO. Significant differences are observed on the proximal face of the protein near the proposed Pdx binding site (*6*, *10*, *11*), including the C helix, the loop containing the heme iron axial ligand (Cys 357), and portions of the L helix. On the distal (active site) side of the heme, the greatest differences are seen in the B′ helix and portions of the I helix that forms one side of the active site. In particular, the region of the I helix directly to the C-terminal side of the I helix "kink" (residues 254−256) shows the largest measured difference between oxidized and reduced CYP101 of any region in the enzyme. The I helix kink (Gly 248−Thr 252) is a distortion of the helix that opens to provide a pocket for Fe-bound dioxygen in the reduced catalytic complex (*12*). Smaller redox-dependent differences in the extent of H−D exchange were also observed in the β-rich region (bottom right-hand portion of Figure 1), including portions of the β3 and β5 strands. With the exception of portions of the N-terminal strand that show some redox-dependent H−D exchange behavior, affected distal regions of the enzyme are all in the proximity of the active site or substrate access pathways.
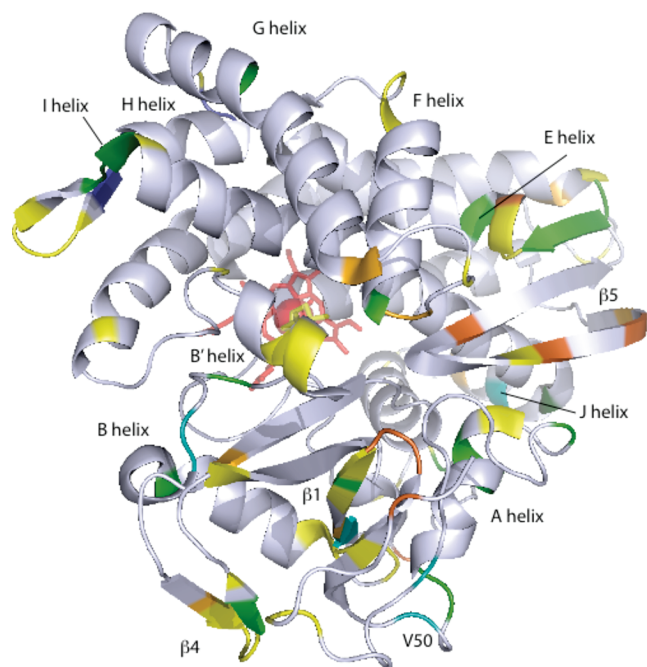
FIGURE 2: Differences in H−D exchange rates determined by NMR superimposed on the 3CPP structure of CYP101 (*25*). Residues are colored according the differences in k_{ex} listed in Table 1. Cooler colors indicate an increased level of local H−D exchange in the oxidized CYP-S relative to reduced CYP-S-CO, with blue showing the largest difference and green indicating measurable differences beyond the 68% confidence level of data fits. Yellow indicates no difference in exchange rates within the confidence level, while orange indicates an increased level of H−D exchange in CYP-S-CO relative to CYP-S. This figure was generated using PyMOL (*26*).

H−D amide proton exchange measurements using NMR provide a complementary view of local redox-dependent dynamics in CYP101. These experiments are performed by measuring the loss of integral intensity of specific amide correlations in 2D ^{1}H−^{15}N TROSY-HSQC during the time course of exchange and obtaining rate constants for exchange from these data. On one hand, these experiments have an advantage over MS-based H−D exchange in being able to localize fluctuations with single-residue resolution. However, a significant drawback of NMR in the measurement of redox-dependent H−D exchange in CYP101 is the inability to compare exchange rates within ∼14.5 Å of the high-spin Fe^{3+} ($S = \frac{5}{2}$) in CYP-S due to paramagnetic broadening of ^{1}H resonances and concomitant loss of ^{1}H−^{15}N correlations in the CYP-S ^{1}H−^{15}N map (although such correlations are readily detected in the diamagnetic CYP-S-CO). Currently, we have assigned 290 (76%) of the 384 non-proline backbone NH groups in CYP-S-CO and have recently published a comprehensive list of CYP-S-CO assignments (*27*). On the basis of these assignments, sufficient comparisons can be made on the basis of the NMR-based H−D exchange experiments to validate and extend the results obtained by MS.

Figure 2 shows the comparison between H−D exchange in oxidized CYP-S and reduced CYP-S-CO graphically on the CYP101 structure. Table 1 provides a list of all H−D exchange rates for CYP-S and CYP-S-CO that could be obtained from the NMR experiments. As with the MS data, oxidized CYP-S shows, with few exceptions, more rapid amide proton exchange than the corresponding residues in CYP-S-CO. Most of the secondary structures that show differences in H−D exchange by MS are not amenable to NMR measurements of H−D exchange due to

paramagnetic broadening in CYP-S. However, where comparisons can be made (such as for the β5 sheet), similar results are obtained from MS and NMR.

The largest measured decrease in the level of H−D exchange upon reduction is observed for Thr 234, at the N-terminus of the I helix. Other significant H−D exchange rate decreases upon reduction occur at Glu 40 (in the first turn of the A helix), Cys 85 (B−B′ loop) Arg 90 (first residue in the B′ helix) Asn 149 (loop between a β5 strand and helix E), Gly 168 (loop between the E and F helices), and Ser 267 and His 270 at the junction between the I and J helices.

There are some local reversals of the trend for more rapid H−D exchange in the oxidized CYP-S than in CYP-S-CO. For example, the amides of residues 384−390, which include a β-turn between two strands of the β5 sheet, show an increase in the H−D exchange rate upon reduction. This is the only cluster of adjacent residues for which this trend can be confirmed, but increases in H−D exchange rates upon reduction are also seen for Arg 143, near the C-terminus of the D helix, Asp 173 (at the N-terminal end of the F helix), Ile 300 (β3 sheet), and Ala 333 (in irregular turn structure connecting the substrate binding site to the β meander). In no case, however, is the difference between CYP-S and CYP-S-CO as pronounced as the most prominent examples of the normal trend.

^{15}*N Relaxation Measurements.* H−D exchange, whether measured by MS or NMR, is sensitive to large-amplitude protein motions with low frequencies (10^{-2} to 10^{-7} s^{-1}). Our reported MS/MS exchange experiments covered a time scale from 10 to 1000 s, corresponding to exchange rate constants of 10^{-2} to 10^{-3} s^{-1}. Reliable rate constants could be obtained only from the current NMR data over a fairly narrow range (∼10^{-5} to 10^{-7} s^{-1}). Conformational sampling faster than 10^{-5} s^{-1} leads to complete exchange within the first time point of NMR H−D exchange experiments. While H−D exchange rates often follow the same trends as local dynamics on shorter time scales (*4, 7, 13, 14*), this is not a given. For this reason, we measured ^{15}N relaxation times (T_1 and T_2) in an effort to correlate the redox dependence of higher-frequency motions in CYP101 with what was observed by H−D exchange. ^{15}N relaxation reflects dynamics on a picosecond to nanosecond time scale, and the ratio of ^{15}N T_1/T_2 can provide qualitative information about motions on other time scales. If the ratio of T_1/T_2 is more than one standard deviation below the mean, large-scale motions on the time scale of hundreds of picoseconds are expected, while deviations above the mean indicate conformational sampling on the millisecond time scale leading to exchange broadening (*15*).

As seen in Figures 3−5, differences in T_2 and T_1/T_2 ratios between CYP-S and CYP-S-CO indicate that the same dynamic trends are evident at shorter times scales as observed by H−D exchange, that is, increased conformational sampling in the oxidized enzyme relative to the reduced CYP-S-CO on the millisecond time scale. The dynamic differences between the oxidized and reduced enzyme detected by ^{15}N relaxation are for the most part found in a cluster on the distal side of the enzyme (Figure 5). The B′ helix and β5 sheet are most uniformly affected (Figure 3), but Ile 300 in the β3 sheet shows the largest measured difference in the T_1/T_2 ratio. Two residues, Glu 209 (G helix) and Val 310 (β4 sheet), show the reverse effect, with T_1/T_2 decreasing in the oxidized enzyme. We note that two of the residues in which H−D exchange is faster in CYP-S-CO than in CYP-S are also located in or adjacent to the β4 sheet.

Table 1: H−D Exchange Rates Measured by NMR in CYP101[a]

	CYP-S (oxidized)		CYP-S-CO (reduced)				CYP-S (oxidized)		CYP-S-CO (reduced)		
residue	k (s^{-1})	error (±)	k (s^{-1})	error (±)	secondary structure	residue	k (s^{-1})	error (±)	k (s^{-1})	error (±)	secondary structure
12	5.2×10^{-6}	2.0×10^{-6}	fast	–		225	–	–	6.0×10^{-6}	4.3×10^{-7}	H helix
17	fast	–	fast	–	turn 1	**226**	**fast**	–	**slow**	–	**H helix**
18	fast	–	fast	–	turn 1	228	fast	–	fast	–	β2
23	fast	–	–	–		229	fast	–	fast	–	β2
24	fast	–	8.1×10^{-7}	4.3×10^{-7}		230	fast	–	fast	–	β2
25	–	–	fast	–		233	2.8×10^{-6}	4.8×10^{-7}	2.5×10^{-6}	4.0×10^{-7}	β2
35	9.0×10^{-7}	4.1×10^{-7}	5.5×10^{-7}	2.2×10^{-7}	**turn 3**	234	4.5×10^{-5}	4.1×10^{-6}	5.7×10^{-6}	7.7×10^{-7}	**I helix**
36	–	–	fast	–	turn 3	235	fast	–	fast	–	I helix
37	fast	–	fast	–	A helix	245	3.0×10^{-6}	7.6×10^{-7}	–	–	I helix
39	9.1×10^{-6}	9.1×10^{-7}	7.3×10^{-6}	4.2×10^{-7}	**A helix**	248	–	–	fast	–	I helix
40	2.1×10^{-5}	1.3×10^{-6}	9.2×10^{-6}	5.3×10^{-7}	**A helix**	249	–	–	fast	–	I helix
47	1.0×10^{-5}	5.9×10^{-7}	7.4×10^{-6}	6.1×10^{-7}	**turn 4**	252	–	–	fast	–	I helix
48	fast	–	–	–	turn 4	253	–	–	fast	–	I helix
50	**fast**	–	8.2×10^{-5}	1.2×10^{-5}	**turn 4**	254	–	–	1.8×10^{-6}	7.1×10^{-7}	I helix
55	slow	–	slow	–	β1	266	7.0×10^{-7}	4.1×10^{-7}	–	–	I helix
59	6.4×10^{-6}	3.2×10^{-6}	fast	–	turn 5	**267**	4.9×10^{-5}	8.5×10^{-6}	2.6×10^{-5}	2.5×10^{-6}	**I helix**
60	fast	–	fast	–	turn 5	**270**	7.6×10^{-7}	4.1×10^{-7}	**slow**	–	**J helix**
61	1.3×10^{-6}	9.0×10^{-8}	8.1×10^{-7}	2.3×10^{-7}	**β1**	271	3.0×10^{-6}	6.6×10^{-7}	–	–	J helix
62	slow	–	slow	–	β1	274	2.2×10^{-6}	3.4×10^{-7}	2.2×10^{-6}	2.3×10^{-7}	J helix
64	9.7×10^{-7}	5.2×10^{-7}	1.6×10^{-6}	5.3×10^{-7}	**β1**	279	fast	–	fast	–	turn 10
65	fast	–	1.3×10^{-6}	8.8×10^{-7}	**β1**	283	4.2×10^{-6}	9.6×10^{-7}	–	–	K helix
67	slow	–	slow	–	B helix	296	–	–	fast	–	β3
68	fast	–	fast	–	B helix	298	–	–	fast	–	β3
70	–	–	9.7×10^{-6}	8.2×10^{-7}	B helix	*300*	3.0×10^{-6}	8.4×10^{-7}	*fast*	–	β3
77	7.2×10^{-6}	4.7×10^{-7}	6.6×10^{-6}	5.7×10^{-7}	**B helix**	302	–	–	1.2×10^{-6}	1.9×10^{-7}	
82	1.9×10^{-6}	1.2×10^{-6}	**slow**	–		304	8.5×10^{-5}	1.5×10^{-5}	–	–	β4
83	–	–	fast	–		306	8.9×10^{-8}	1.5×10^{-6}	fast	–	β4
85	1.8×10^{-5}	1.6×10^{-6}	5.1×10^{-6}	4.1×10^{-7}		307	fast	–	fast	–	turn 11
87	–	–	fast	–		308	fast	–	fast	–	turn 11
88	–	–	fast	–		309	fast	–	fast	–	turn 11
90	fast	–	fast	–	B′ helix	**310**	3.3×10^{-6}	4.7×10^{-7}	2.8×10^{-6}	2.5×10^{-7}	**turn 11**
91	fast	–	fast	–	B′ helix	312	slow	–	slow	–	β4
92	–	–	2.0×10^{-6}	8.3×10^{-7}	B′ helix	313	1.8×10^{-6}	4.7×10^{-7}	–	–	β4
93	fast	–	fast	–	B′ helix	314	–	–	1.7×10^{-6}	3.0×10^{-7}	β3
94	–	–	fast	–	B′ helix	315	fast	–	fast	–	β3
96	1.9×10^{-6}	6.3×10^{-7}	–	–	B′ helix	326	–	–	fast	–	
98	fast	–	fast	1.4×10^{-6}	turn 6	329	fast	–	fast	–	turn 12
99	–	–	fast	1.8×10^{-6}	turn 6	330	–	–	–	–	turn 12
107	fast	–	fast	1.5×10^{-6}	turn 7	333	3.1×10^{-6}	1.1×10^{-6}	fast	–	turn 13
118	–	–	2.8×10^{-6}	9.4×10^{-7}	C helix	334	fast	–	fast	–	turn 13
119	–	–	5.2×10^{-6}	4.3×10^{-7}	C helix	338	fast	–	–	–	
120	–	–	6.2×10^{-5}	1.7×10^{-5}	C helix	**339**	6.1×10^{-6}	1.1×10^{-6}	3.1×10^{-6}	6.5×10^{-7}	
124	1.8×10^{-6}	1.2×10^{-6}	–	–	C helix	340	fast	–	fast	–	
143	3.6×10^{-6}	4.9×10^{-7}	10.0×10^{-6}	1.9×10^{-6}	*D helix*	342	fast	–	fast	–	
145	fast	–	2.1×10^{-5}	2.0×10^{-6}	β5	348	–	–	fast	–	turn 14
146	2.5×10^{-5}	3.7×10^{-6}	2.1×10^{-5}	2.0×10^{-6}	**β5**	349	–	–	fast	–	turn 14
147	2.7×10^{-6}	4.1×10^{-7}	2.1×10^{-6}	2.2×10^{-7}	**β5**	351	–	–	fast	–	turn 14
148	3.0×10^{-6}	4.0×10^{-7}	2.0×10^{-6}	2.9×10^{-7}	**β5**	354	–	–	fast	–	turn 15
149	2.1×10^{-5}	6.3×10^{-6}	6.1×10^{-6}	6.6×10^{-7}	**β5**	356	–	–	fast	–	turn 15
150	9.7×10^{-6}	7.6×10^{-7}	4.6×10^{-6}	4.8×10^{-7}	**β5**	357	–	–	5.3×10^{-6}	9.0×10^{-7}	
151	fast	–	fast	–	E helix	358	–	–	fast	–	
152	1.1×10^{-5}	4.5×10^{-6}	fast	–	E helix	369	slow	–	–	–	L helix
154	6.7×10^{-6}	7.5×10^{-7}	5.1×10^{-6}	8.6×10^{-7}	**E helix**	376	–	–	5.6×10^{-6}	1.0×10^{-6}	L helix
168	4.9×10^{-5}	5.8×10^{-6}	2.5×10^{-5}	6.7×10^{-6}		*384*	2.2×10^{-5}	4.5×10^{-6}	2.6×10^{-5}	2.5×10^{-6}	*turn 16*
171	fast	–	–	–	turn 8	*386*	6.5×10^{-7}	4.4×10^{-7}	*fast*	–	*turn 16*
172	fast	–	fast	–	turn 8	*387*	4.4×10^{-6}	5.5×10^{-7}	*fast*	–	*turn 16*
173	fast	–	fast	–	F helix	388	5.7×10^{-6}	1.0×10^{-6}	–	–	β5
185	1.7×10^{-5}	1.2×10^{-6}	1.4×10^{-5}	1.0×10^{-6}		390	2.4×10^{-6}	1.5×10^{-6}	*fast*	–	β5
186	4.4×10^{-6}	7.6×10^{-7}	4.8×10^{-6}	4.9×10^{-7}		391	fast	–	fast	–	β5
188	–	–	fast	–		392	1.8×10^{-6}	2.9×10^{-7}	–	–	β5
189	fast	–	fast	–		394	–	–	fast	–	β5
192	1.3×10^{-6}	4.3×10^{-7}	*fast*	–	*G helix*	396	–	–	fast	–	β5
195	1.8×10^{-5}	3.7×10^{-6}	–	–	G helix	398	3.3×10^{-7}	4.3×10^{-7}	fast	–	β5
196	–	–	7.2×10^{-6}	6.3×10^{-7}	G helix	400	–	–	fast	–	β5
199	1.9×10^{-6}	2.6×10^{-7}	–	–	G helix	401	8.6×10^{-6}	7.5×10^{-7}	–	–	β5
200	fast	–	–	–	G helix	410	fast	–	fast	–	
207	1.1×10^{-5}	8.2×10^{-7}	1.1×10^{-5}	8.9×10^{-7}	G helix	411	–	–	9.4×10^{-7}	1.1×10^{-7}	
209	2.5×10^{-5}	4.7×10^{-6}	–	–	G helix	412	–	–	fast	–	
216	fast	–	fast	–	H helix	413	–	–	fast	–	
217	**fast**	–	**slow**	–	**H helix**	414	fast	–	fast	–	

[a] A blank entry under exchange rate (k) indicates that either the peak is missing in the oxidized form due to paramagnetic broadening or no accurate integral measurements were possible due to spectral overlap. Error values are differences between reported values and 68% confidence level values as described in the text. Residues highlighted in bold show slower exchange in the reduced form than in the oxidized form, and those highlighted in italics are slower in the oxidized form.
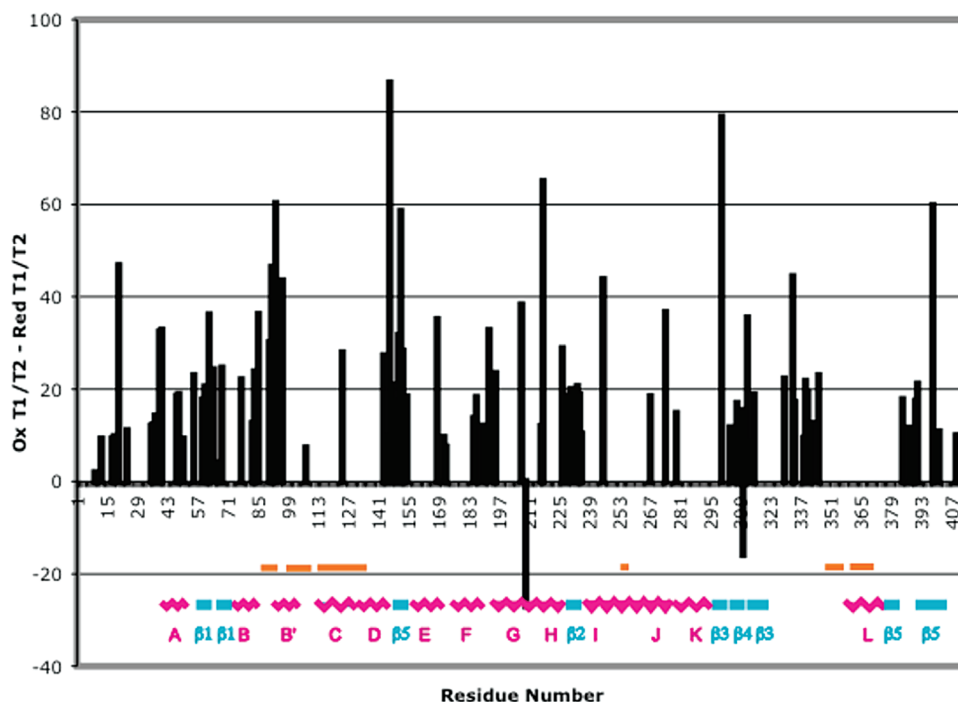
FIGURE 3: Differences in ^{15}N T_1/T_2 ratios between oxidized (CYP-S) and reduced (CY-S-CO) CYP101 as a function of sequence. Secondary structural features are indicated by colored graphics, labeled using the scheme of Ragg and Poulos (*25*). Differences are superimposed via color shading on the CYP101 structure in Figure 5. Orange bars indicate regions where significant differences in H−D exchange are detected by mass spectrometry. Error estimates for individual ^{15}N relaxation measurements can be found in the Supporting Information.
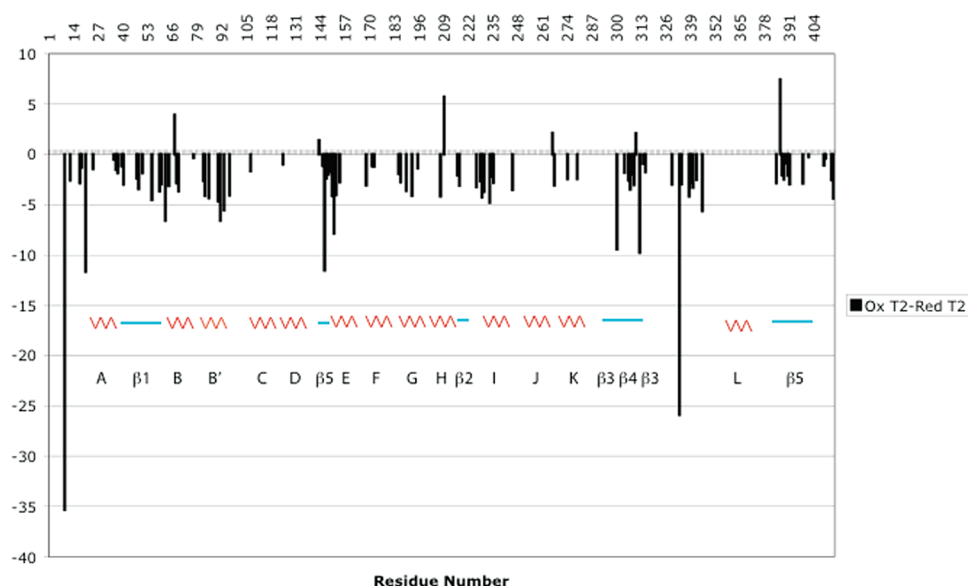
FIGURE 4: Differences in ^{15}N T_2 values between oxidized (CYP-S) and reduced (CY-S-CO) CYP101. Secondary structural features are indicated by colored graphics, labeled using the scheme of Ragg and Poulos (*25*). Error bars are shown for individual T_1 and T_2 measurements in the Supporting Information.

A concern arising from the use of ^{15}N relaxation methods in examining dynamics in CYP101 is the dramatically different electronic environment of the heme between the two forms of the enzyme. CYP-S-CO is diamagnetic (Fe^{2+}; $S = 0$), and electron−nuclear spin interactions do not affect nuclear spin relaxation. The oxidized CYP-S is almost completely high-spin (Fe^{3+}; $S = {}^5/_2$). This results in electron−nuclear spin interactions that broaden ^1H resonances beyond detectability within ∼14.5 Å of the heme iron. However, as ^{15}N is ∼100-fold less susceptible than ^1H to paramagnetic relaxation effects as a function of distance from the paramagnetic center, it is reasonable to assume that if

the ^1H of an NH pair is detectable in CYP-S, the relaxation behavior of the attached ^{15}N will not be significantly affected by paramagnetism. This assumption is supported by the lack of any discernible relationship between measured ^{15}N T_1 and T_2 values (see the Supporting Information) and the distance between the heme iron and corresponding ^{15}N spin in CYP-S.

DISCUSSION

The results of H−D exchange and ^{15}N relaxation measurements described here combined with previously published MS
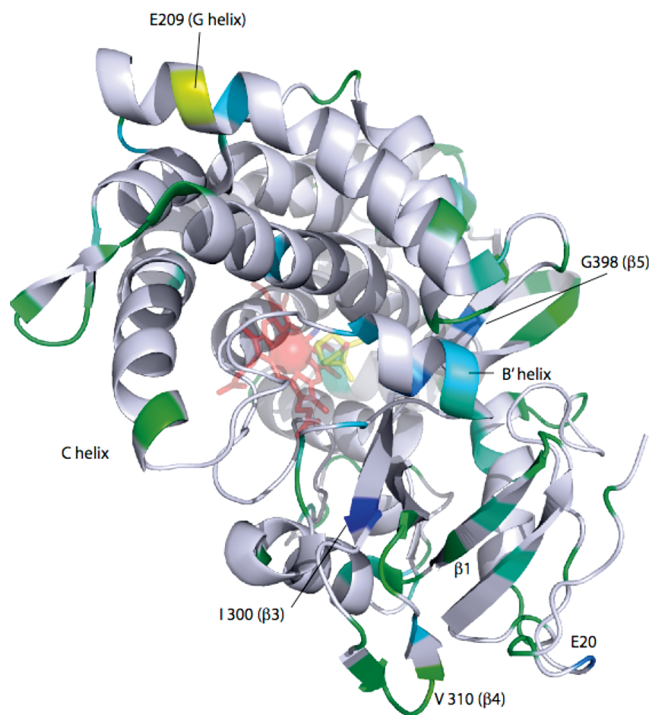
FIGURE 5: Differences in millisecond time scale dynamics as reflected by ^{15}N T_1/T_2 ratios superimposed on the 3CPP structure of CYP101 (25). Cooler colors indicate increased local dynamics in the oxidized CYP-S relative to reduced CYP-S-CO, with blue showing the greatest difference and green the smallest. Yellow indicates increased dynamics in CYP-S-CO relative to CYP-S (see the text). This figure was generated using PyMOL (26).

data provide a consistent and complementary picture of redox-dependent dynamics in CYP101. For example, all three types of experiments indicate that the dynamics of the $\beta 5$ sheet, which is involved in active site access and substrate orientation in the active site, is sensitive to oxidation state on all accessible time scales. The B$'$ helix, which transmits conformational changes upon binding of Pdx to CYP-S-CO at the C helix to the active site and other distal positions, is seen to change dynamics from both the relaxation measurements and MS H/D exchange.

While reduced CYP-S-CO shows lower-amplitude motions on all accessible time scales than oxidized CYP-S in most cases, there are interesting exceptions to this trend. In the NMR-based H−D exchange experiments, most residues in the $\beta 5$ sheet show a decreased exchange rate in CYP-S-CO relative to CYP-S. However, one cluster of residues, Ala 384−Gln 390, which includes a turn linking two strands of the $\beta 5$ sheet, shows increased H−D exchange rates in reduced CYP-S-CO relative to the oxidized form, suggesting that increased amplitude motion within the $\beta 5$ sheet in CYP-S is at least partially compensated by decreasing the amplitude of such motions near the edges of the sheet. We observed a similar phenomenon when we compared H−D exchange in oxidized and reduced Pdx (4).

Motional differences on the millisecond time scale are detected by differences in the ratio of ^{15}N T_1/T_2 as a function of oxidation state. From Figure 5, the largest effects of this type are seen in the distal cluster of secondary structural features, including the B$'$ helix and portions of the $\beta 3$ and $\beta 5$ sheets, with smaller effects in the I helix and $\beta 1$ sheet. This clustering suggests that at least some of the motions responsible for the observed effects are coordinated not only within a given secondary structure but also between secondary structural features. Furthermore, since some

of these same features must be distorted or displaced to open the substrate access channel (16, 17), these results suggest that the active site is more accessible on the millisecond time scale in oxidized CYP-S than in CYP-S-CO.

That CPY-S is generally more dynamic than reduced CYP-S-CO is, in itself, not surprising. With few exceptions (18), this trend has been observed for redox-active metalloproteins regardless of the type of metal center involved (4, 19, 20). What is intriguing, however, is the localization of the dynamic differences in CYP101. The largest differences in dynamics, as determined by H−D exchange, are located on the proximal face in the proposed Pdx binding site and, on the distal side, in secondary structural features adjacent to the active site and regions implicated in gating substrate access to the active site. In particular, the B$'$ helix is less dynamic in CYP-S-CO than in CYP-S both in the MS H−D exchange and ^{15}N relaxation experiments. The B$'$ helix provides a critical mechanical link between the proximal Pdx binding site (formed in part by helix C, helix L, and the axial Cys 357 loop) and the distal regions most affected by Pdx binding, including the I helix and the B−B$'$ loop. The B$'$ helix begins at Pro 89 and is one of the secondary structural features implicated in gating substrate access to the CYP101 active site. We recently proposed that isomerization of the Ile 88-Pro 89 amide bond is the critical "switch" driven by binding of Pdx that reorients the substrate camphor in the active site appropriately for the observed chemistry (5). Given that the spectral changes associated with the isomerization are not observed upon binding of Pdx to oxidized CYP-S, it is clear that reduction of CYP101 is required for the isomerization to occur.

Due to paramagnetic broadening of resonances near the heme in CYP-S, it is not possible from the current data to propose a mechanism for the observed relationship between protein dynamics and oxidation state in CYP101. What insight we have comes from the related case of redox-dependent dynamics in Pdx. We found that mutation of a histidine residue (His 49) structurally and sequentially adjacent to the redox-active metal cluster essentially abolished the sensitivity of protein dynamics to metal center oxidation state in Pdx, and we proposed that His 49 acts as a mechanical linkage, transmitting redox-induced conformational changes in the polypeptide surrounding the metal center to other regions of the protein via hydrogen bonding interactions (14). A similar case could be made in the case of CYP101 for His 355, which forms a salt bridge with a heme propionate via the Nδ atom of imidazole. Nε of His 355 is within hydrogen bonding or salt bridge distance of residues in the B−B$'$ loop (Ser 83 Oγ), the B$'$−C loop (Met 103 carbonyl oxygen), and the C helix (Glu 108 carboxylate). All of these secondary structural features exhibit redox-dependent dynamics in the experiments described here or previously by MS/MS, so it is possible that changes in the heme iron oxidation state result in changes in charge distribution in this network of salt bridges and hydrogen bonds, changes which are then transmitted to other affected areas of the enzyme. However, mutations of His 355 to Phe, Asp, and Asn resulted in destabilization of the enzyme, so the importance of this residue to redox-dependent dynamics of CYP101 could not be confirmed (5).

SUPPORTING INFORMATION AVAILABLE

Table of calculated ^{15}N T_1 and T_2 values, examples of fits of H−D exchange data, ^{15}N T_1 and T_2 values with error bars as a function of sequence, annotated TROSY-HSQC spectrum for

CYP-S-CO, and overlay of TROSY-HSQC spectra of CYP-S (oxidized) and CYP-S-CO (reduced). This material is available free of charge via the Internet at http://pubs.acs.org.

REFERENCES

1. Ju, T. T., Goldsmith, R. B., Chai, S. C., Maroney, M. J., Pochapsky, S. S., and Pochapsky, T. C. (2006) One protein, two enzymes revisited: A structural entropy switch interconverts the two isoforms of acireductone dioxygenase. *J. Mol. Biol. 363*, 523–534.

2. Leitch, S., Bradley, M. J., Rowe, J. L., Chivers, P. T., and Maroney, M. J. (2007) Nickel-specific response in the transcriptional regulator, *Escherichia coli* NikR. *J. Am. Chem. Soc. 129*, 5085–5095.

3. Hidalgo, E., and Demple, B. (1994) An iron-sulfur center essential for transcriptional activation by the redox-sensing SoxR protein. *EMBO J. 13*, 138–146.

4. Lyons, T. A., Ratnaswamy, G., and Pochapsky, T. C. (1996) Redox-dependent dynamics of putidaredoxin characterized by amide proton exchange. *Protein Sci. 5*, 627–639.

5. OuYang, B., Pochapsky, S. S., Dang, M., and Pochapsky, T. C. (2008) A functional proline switch in cytochrome P450(cam). *Structure 16*, 916–923.

6. Pochapsky, S. S., Pochapsky, T. C., and Wei, J. W. (2003) A model for effector activity in a highly specific biological electron transfer complex: The cytochrome P450(cam)-putidaredoxin couple. *Biochemistry 42*, 5649–5656.

7. Pochapsky, T. C., Kostic, M., Jain, N., and Pejchal, R. (2001) Redox-dependent conformational selection in a Cys$_4$Fe$_2$S$_2$ ferredoxin. *Biochemistry 40*, 5602–5614.

8. Hamuro, Y., Molnar, K. S., Coales, S. J., OuYang, B., Simorellis, A. K., and Pochapsky, T. C. (2008) Hydrogen-deuterium exchange mass spectrometry for investigation of backbone dynamics of oxidized and reduced cytochrome P450cam. *J. Inorg. Biochem. 102*, 364–370.

9. Englander, S. W. (2000) Protein folding intermediates and pathways studied by hydrogen exchange. *Annu. Rev. Biophys. Biomol. Struct. 29*, 213–238.

10. Koga, H., Sagara, Y., Yaoi, T., Tsujimura, M., Nakamura, K., Sekimizu, K., Makino, R., Shimada, H., Ishimura, Y., Yura, K., Go, M., Ikeguchi, M., and Horiuchi, T. (1993) Essential role of the Arg112 residue of cytochrome-P450cam for electron transfer from reduced putidaredoxin. *FEBS Lett. 331*, 109–113.

11. Pochapsky, T. C., Lyons, T. A., Kazanis, S., Arakaki, T., and Ratnaswamy, G. (1996) A structure-based model for cytochrome P450(cam)-putidaredoxin interactions. *Biochimie 78*, 723–733.

12. Poulos, T. L., Finzel, B. C., and Howard, A. J. (1987) High resolution crystal-structure of cytochrome P450cam. *J. Mol. Biol. 195*, 687–700.

13. Sari, N., Holden, M. J., Mayhew, M. P., Vilker, V. L., and Coxon, B. (1999) Comparison of backbone dynamics of oxidized and reduced putidaredoxin by N-15 NMR relaxation measurements. *Biochemistry 38*, 9862–9871.

14. Kostic, M., Bernhardt, R., and Pochapsky, T. C. (2003) A conserved histidine in vertebrate-type ferredoxins is critical for redox-dependent dynamics. *Biochemistry 42*, 8171–8182.

15. Clore, G. M., Driscoll, P. C., Wingfield, P. T., and Gronenborn, A. M. (1990) Analysis of the backbone dynamics of interleukin-1-β using 2-dimensional inverse detected heteronuclear ^{15}N-^{1}H NMR spectroscopy. *Biochemistry 29*, 7387–7401.

16. Ludemann, S. K., Lounnas, V., and Wade, R. C. (2000) How do substrates enter and products exit the buried active site of cytochrome P450cam? 1. Random expulsion molecular dynamics investigation of ligand access channels and mechanisms. *J. Mol. Biol. 303*, 797–811.

17. Ludemann, S. K., Lounnas, V., and Wade, R. C. (2000) How do substrates enter and products exit the buried active site of cytochrome P450cam? 2. Steered molecular dynamics and adiabatic mapping of substrate pathways. *J. Mol. Biol. 303*, 813–830.

18. Blanchard, L., Blackledge, M. J., Marion, D., and Guerlesquin, F. (1996) Investigation of oxidation state-dependent conformational changes in *Desulfovibrio vulgaris* Hildenborough cytochrome c(553) by two-dimensional ^{1}H-NMR spectra. *FEBS Lett. 389*, 203–209.

19. Gooley, P. R., Zhao, D. Z., and MacKenzie, N. E. (1991) Comparison of amide proton exchange in reduced and oxidized *Rhodobacter capsulatus* cytochrome c2: A ^{1}H-^{15}N NMR study. *J. Biomol. NMR 1*, 145–154.

20. Marmorino, J. L., Auld, D. S., Betz, S. F., Doyle, D. F., Young, G. B., and Pielak, G. J. (1993) Amide proton exchange rates of oxidized and reduced *Saccharomyces cerevisiae* iso-1-cytochrome c. *Protein Sci. 2*, 1966–1974.

21. Rui, L. Y., Pochapsky, S. S., and Pochapsky, T. C. (2006) Comparison of the complexes formed by cytochrome P450(cam) with cytochrome b(5) and putidaredoxin, two effectors of camphor hydroxylase activity. *Biochemistry 45*, 3887–3897.

22. Nickerson, D. P., and Wong, L. L. (1997) The dimerization of *Pseudomonas putida* cytochrome P450(cam): Practical consequences and engineering of a monomeric enzyme. *Protein Eng. 10*, 1357–1361.

23. Pervushin, K., Riek, R., Wider, G., and Wuthrich, K. (1997) Attenuated T$_2$ relaxation by mutual cancellation of dipole-dipole coupling and chemical shift anisotropy indicates an avenue to NMR structures of very large biological macromolecules in solution. *Proc. Natl. Acad. Sci. U.S.A. 94*, 12366–12371.

24. Zhu, G., Xia, Y. L., Nicholson, L. K., and Sze, K. H. (2000) Protein dynamics measurements by TROSY-based NMR experiments. *J. Magn. Reson. 143*, 423–441.

25. Raag, R., and Poulos, T. L. (1989) Crystal structure of the carbon monoxide substrate cytochrome P450cam ternary complex. *Biochemistry 28*, 7586–7592.

26. DeLano, W. L. (2008) *The PyMOL molecular graphics system*, DeLano Scientific, San Carlos, CA.

27. Asciutto, E. K., Madura, J. D., Pochapsky, S. S., OuYang, B., and Pochapsky, T. C. (2009) Structural and dynamic implications of an effector-induced backbone amide cis-trans isomerization in cytochrome P450cam. *J. Mol. Biol.* (in press).